# Plasma frequency in doped highly mismatched alloys

Hassan Allami
*Department of Physics, University of Ottawa, Ottawa, Ontario, Canada K1N 6N5*

Jacob J. Krich
*Department of Physics and School of Electrical Engineering and Computer Science, University of Ottawa, Ottawa, Ontario, Canada K1N 6N5*

(Received 29 October 2020; revised 9 December 2020; accepted 14 December 2020; published 7 January 2021)

Highly mismatched alloys (HMAs) have band structures strongly modified due to the introduction of the alloying element. We consider HMAs where the isolated state of the alloying element is near the host conduction band, which causes the conduction band to split into two bands. We determine the bulk plasma frequency when the lower-energy band is partially occupied, as by doping, using a semianalytical method based on a disorder-averaged Green's function. We include the nontrivial effects of interband transitions to the higher-energy band, which limit the plasma frequency to be less than an effective band gap. We show that the distribution of states in the split bands causes plasmons in HMAs to behave differently than plasmons in standard metals and semiconductors. The effective mass of the lower split band $m^*$ changes with alloy fraction, and we find that the plasmon frequency with small carrier concentration $n$ scales with $\sqrt{n}/m^*$ rather than the $\sqrt{n/m^*}$ that is expected in standard materials. We suggest experiments to observe these phenomena. Considering the typical range of material parameters in this group of alloys and taking a realistic example, we suggest that HMAs can serve as highly tunable low-frequency plasmonic materials.

DOI: 10.1103/PhysRevB.103.035201

## I. INTRODUCTION

Highly mismatched alloys (HMAs) are semiconductor compounds in which atoms of significantly different electronegativity substitute the host atoms. They are characterized by an unusually strong variation in their fundamental band gap upon the introduction of a small fraction of substituting elements. The band anticrossing (BAC) model was proposed to explain this behavior [1]. In the BAC model, the highly mismatched substitute atoms form localized states with energy $E_d$ near the continuum of extended states of the host material, $E_{\mathbf{k}}$. The localized states strongly couple to the host's extended states, leading to the formation of two split bands, $E_\pm$ [see Figs. 1(a) and 2(a)].

The dramatic band-gap drop, first observed in the 1990s [2], soon found applications such as developing quantum well laser diodes [3] and high-efficiency multijunction solar cells [4]. Later, building on the BAC model of two split bands in HMAs, they were used to implement intermediate-band solar cells [5–11], which is another scheme for harvesting sub-band-gap photons [12]. A collection of recent developments in the study of this class of semiconductor alloys can be found in Ref. [13].

The plasmonic properties of the split bands in HMAs have not been studied. As with any band, the presence of mobile charge carriers results in a negative dielectric function below and near the resonant plasma frequency of the medium. The interface of such a medium with a surrounding dielectric supports localized surface modes that are the basis of plasmonic phenomena such as the subwavelength walking waves of surface plasmon polaritons [14] or the standing modes of localized surface plasmons on nanoparticles [15]. The operating frequency range of these modes is determined by the bulk plasma frequency $\omega_p$ of the system. While the classic plasmonic metals such as gold and silver have operating frequencies in the visible and near-infrared range, there has been a search for alternative plasmonic materials that operate in lower frequency ranges, such as terahertz and mid-infrared, which can offer technological advantages such as reducing the size of electronic devices operating in these ranges [16].

While doping of HMA bands can be a challenge [17], mobile charge in the $E_-$ band can provide tunable plasmonic effects. We show that both the origins of that band and the close proximity to the $E_+$ band make these properties different from standard doped semiconductor plasmonics [18]. As with doped semiconductors, the carrier density in such a system is low compared to noble metals, giving a lower frequency range of plasmonic operation. The large tunability of both band gaps and doping in HMAs makes them appealing platforms for development of plasmonic structures in the mid-infrared regime. These plasma oscillations may also be important for recombination in HMA-based intermediate-band solar cells. Moreover, since a gap separates the $E_-$ band from the $E_+$ band, proper tuning could allow for minimizing loss, which is a crucial favorable feature for plasmonic applications [19].

In this work, we study the long-wavelength limit of bulk plasmons of a model for HMAs. In particular, we focus on the important role of state distribution, which is beyond the scope of the simpler BAC model. We show that since the state distribution between the BAC bands and the effective mass of

 

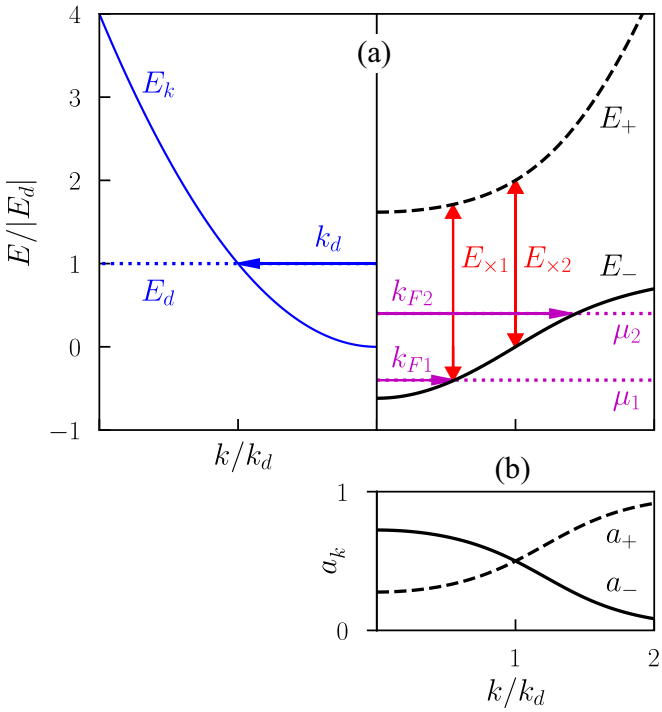


FIG. 1. (a) Band structure of a generic HMA with $E_d > 0$ and (b) corresponding weighting factors. (a, left) Impurity level, $E_d$, and conduction band of the host material, which is taken to be parabolic, $E_{\mathbf{k}} = k^2/2m$. The $k$ axes are normalized to $k_d$, defined in Eq. (5) and also indicated. The energy axis is normalized to $|E_d|$. (a, right) The corresponding two split bands of the BAC, $E_\pm$, according to Eq. (2), for $V^2 x = E_d^2$. Also, for the two different cases of Eq. (9), two different levels of filling are shown by $\mu$'s and $k_F$'s, with their corresponding interband energy gaps, $E_{\times 1}$ and $E_{\times 2}$. (b) Weighting factors $a_\pm$ for this realization, from Eq. (7).

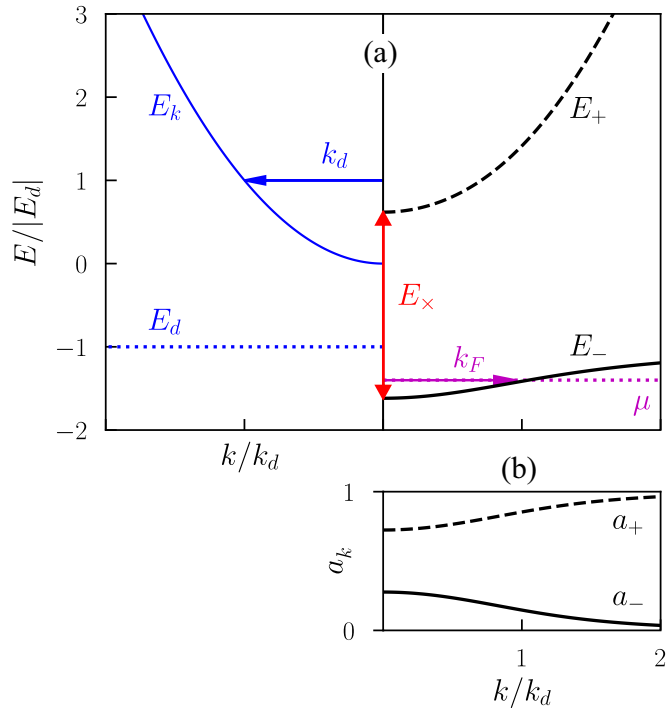


FIG. 2. (a) Band structure of a generic HMA with $E_d < 0$ and (b) corresponding weighting factors. (a, left) Impurity level, $E_d$, and conduction band of the host material, which is taken to be parabolic. The $k$ axes are normalized to $k_d$, defined in Eq. (5), and also indicated. (a, right) The corresponding two split bands of BAC, $E_\pm$, according to Eq. (2), for $V^2 x = E_d^2$. A chemical potential, $\mu$, and its corresponding $k_F$ are also shown, along with the interband energy gap, $E_\times$, which is independent of filling when $E_d < 0$. (b) Weighting factors $a_\pm$ for this realization, from Eq. (7).

the lower $E_-$ band both depend on alloy fraction, the resulting plasma frequency does not have the standard $\sqrt{4\pi n e^2/m^*}$ form, where $n$ is carrier density, $m^*$ is effective mass, and $e$ is the fundamental charge, even in the dilute limit where the $E_-$ band is well approximated as parabolic. In Sec. II we formulate the calculation of the density susceptibility of the system in the long-wavelength limit, which is required for finding $\omega_p$ of the system. Next, in Sec. III we set up an equation for $\omega_p$ of the system and analyze the behavior of its solution, emphasizing the important qualitative features. Finally in Sec. IV, we provide numerical values for $\omega_p$ for typical realistic parameters of previously studied HMAs and conclude by commenting on experimental methods for observing the predicted phenomena.

## II. SUSCEPTIBILITY OF HMA BANDS

In this section, we construct a formulation for calculating the susceptibility that is needed to find the plasma frequency of a HMA system. First we show how the state distribution is described by the spectral density of the system, and then we use it in the calculation of susceptibility $\chi$. We show how the formulation simplifies in the long-wavelength limit and derive the limiting form to be used for our semianalytical calculations.

### A. The spectral density of HMAs

The BAC model considers only the localized impurity levels with energy $E_d$ and one set of extended states of the host material, $E_{\mathbf{k}}$, which we consider to be the conduction band (CB) of the host material. The BAC model introduces a $2 \times 2$ Hamiltonian at each wave vector $\mathbf{k}$ [1],

$$H_{\mathrm{BAC}} = \begin{bmatrix} E_{\mathbf{k}} & V\sqrt{x} \\ V\sqrt{x} & E_d \end{bmatrix}, \tag{1}$$

where $V$ is the average coupling between localized and extended levels, and $x$ is the fraction of impurity atoms. This matrix can be diagonalized to give two split bands with energies

$$E_{\mathbf{k}}^{\pm} = \frac{1}{2}\left(E_{\mathbf{k}} + E_d \pm \sqrt{(E_{\mathbf{k}} - E_d)^2 + 4V^2 x}\right). \tag{2}$$

Measuring energy from the bottom of the CB of the host material, we identify two cases: when the impurity level is inside the CB, $E_d > 0$, as in Fig. 1(a), and when the impurity level is below the band edge of the CB, $E_d < 0$, as in Fig. 2(a).

While this model provides a good description of the energy spectrum of HMAs, it does not preserve the total number of states, as it implies two $\mathbf{k}$ states for each extended $\mathbf{k}$ state of the host material, which is incorrect for small $x$. Early in the development of the BAC model, Wu *et al.*, based on

Anderson's impurity model [20], proposed an average Green's function

$$G(E,\mathbf{k}) = \left[E - E_{\mathbf{k}} - \frac{V^2 x}{E - E_d + i\Gamma}\right]^{-1}, \tag{3}$$

which does not suffer from this issue [21]. Here, $\mathbf{k}$ is still a good quantum number in the ensemble average sense [22]. In this Green's function, $\Gamma$ is a broadening factor given by $\pi\beta V^2\rho_0(E_d)$, where $\rho_0(E_d)$, which has dimensions of inverse energy, is the unperturbed density of states in a unit cell at the energy of the defect level, and $\beta$ is a number of the order of 1.

As we show, the distribution of states with energy plays an important role in the dynamics of bulk plasmons in HMAs. The spectral density of a Green's function properly describes the distribution of states in a system. It is well known that the spectral density (or spectral function) of a retarded Green's function is given by $A_{\mathbf{k}}(E) = -\mathrm{Im}[G(E,\mathbf{k})]/\pi$, from which the HMA spectral function is

$$A_{\mathbf{k}}(E) = \frac{1}{\pi}\frac{\Gamma V^2 x}{[(E - E_d)(E - E_{\mathbf{k}}) - V^2 x]^2 + \Gamma^2(E - E_{\mathbf{k}})^2}. \tag{4}$$

One can check that for each $\mathbf{k}$, the integral of $A_{\mathbf{k}}(E)$ in Eq. (4) over energy equals 1; $A_{\mathbf{k}}(E)$ describes how each $\mathbf{k}$ is distributed among all energies due to hybridization of the localized and propagating states. Note that when the broadening factor $\Gamma$ is sufficiently small, the spectral density in Eq. (4) has two sharp peaks near the split bands of the BAC model, $E_{\mathbf{k}}^{\pm}$ in Eq. (2), as they are the roots of the square bracket in the denominator of $A_{\mathbf{k}}(E)$. This relationship shows how the Green's function in Eq. (3) contains the BAC model.

The broadening factor $\Gamma$ is naturally much smaller than $V$, most obviously when $E_d < 0$, in which case $\Gamma = 0$. Consider a parabolic host CB and define $k_d$ such that $E_{k_d} = |E_d|$, as illustrated in Figs. 1(a) and 2(a), giving

$$k_d = \frac{\sqrt{2m|E_d|}}{\hbar}. \tag{5}$$

Then in the $E_d > 0$ case, approximating the size of the unit cell by $k_{\mathrm{BZ}}^{-3}$, where $k_{\mathrm{BZ}}$ is the length of the Brillouin zone, we have $\rho_0(E_d) \approx mk_d k_{\mathrm{BZ}}^{-3}/(\hbar\pi)^2$. We also introduce an equivalent momentum for the coupling factor, $k_V = \sqrt{2mV}/\hbar$, and find $\Gamma/V \approx \beta k_d k_V^2/(2\pi k_{\mathrm{BZ}}^3)$. Then, since $k_d \ll k_{\mathrm{BZ}}$ and $k_V \lesssim k_{\mathrm{BZ}}$ (since $V$ is of the order of eV), we still have $\Gamma \ll V$. For instance, Heyman *et al.* used $\Gamma = 10^{-3}V$ in modeling their measurements of samples of $GaN_xP_yAs_{1-y-x}$ (see Table I in Ref. [9]).

On this basis, we consider the limit $\Gamma \to 0$, where the spectral density in Eq. (4) turns into two weighted $\delta$ functions centered at the split bands of the BAC model, $E_{\mathbf{k}}^{\pm}$ in Eq. (2), indicating the share of each one at a given $\mathbf{k}$:

$$A_{\mathbf{k}}(E) = a_{\mathbf{k}}^{-}\delta(E - E_{\mathbf{k}}^{-}) + a_{\mathbf{k}}^{+}\delta(E - E_{\mathbf{k}}^{+}), \tag{6}$$

where the weighting factors are given by

$$a_{\mathbf{k}}^{\pm} = \frac{V^2 x}{|E_{\mathbf{k}}^{\pm} - E_{\mathbf{k}}|(E_{\mathbf{k}}^{+} - E_{\mathbf{k}}^{-})}. \tag{7}$$

One can check that at any given $\mathbf{k}$ the expressions in Eq. (7) satisfy $a_{\mathbf{k}}^{-} + a_{\mathbf{k}}^{+} = 1$, as expected.

These weighting factors $a_{\mathbf{k}}^{\pm}$ are shown in Figs. 1(b) and 2(b). Notice that $a_{\mathbf{k}}^{-}$ has its maximum at $k = 0$ and that in the case of $E_d > 0$, it is larger than $a_k^{+}$ for $k < k_d$, while in the case of $E_d < 0$, it is always smaller than $a_k^{+}$.

### B. Long-wavelength limit of the susceptibility

We use the Green's function of Eq. (3) and the spectral density in the limit of small $\Gamma$, Eq. (6), to construct the susceptibility, dielectric function, and plasma frequency of an HMA described by Eq. (3) at zero temperature. We consider the case where doping ensures the chemical potential is in the $E_-$ band. We assume the valence band lies far below the chemical potential and can be ignored. In this model, $E_{\mathbf{k}}$, $E_d$, and $V$ are fixed parameters of the material. The alloy fraction, $x$, can be tuned, and doping controls chemical potential $\mu$. Since the model is isotropic, we parametrize the chemical potential using the Fermi momentum, $k_F$. Two examples of $E_{\pm}$ with $E_d$ above and below zero are shown in Figs. 1 and 2. Also shown is the effective interband energy gap, $E_{\times}$, which is the smallest difference in energy between an $E_+$ state and an occupied $E_-$ state at the same $\mathbf{k}$:

$$E_{\times} = \min_{k<k_F}(E_{\mathbf{k}}^{+} - E_{\mathbf{k}}^{-}). \tag{8}$$

As shown in Fig. 2, when $E_d < 0$ we always have $E_{\times} = \sqrt{E_d^2 + 4V^2 x}$, regardless of the filling of $E_-$, as the minimum gap occurs at $k = 0$. For $E_d > 0$ however, as in Fig. 1, we have

$$E_{\times} = \begin{cases} \sqrt{(E_d - E_{k_F})^2 + 4V^2 x}, & k_F < k_d \\ 2V\sqrt{x}, & k_F \geqslant k_d, \end{cases} \tag{9}$$

since the minimum value of $(E_{\mathbf{k}}^{+} - E_{\mathbf{k}}^{-})$ occurs at $k = k_d$.

Bulk plasmons of this system are rooted in the collective density oscillations of free electrons due to electron-electron interactions in the $E_-$ band. This resonant mode can be seen as an instability when the real part of the dielectric function $\epsilon$ equals zero. The plasma frequency $\omega_p$ of the system is the frequency associated to the long-wavelength limit of this resonance. Therefore, to compute $\omega_p$ we need a suitable expression for $\epsilon$. The well-known random phase approximation (RPA) allows consideration of electron-electron interactions. The RPA is exact in the high-density limit and often qualitatively accurate even at relatively low carrier concentrations. The standard RPA relation connects the density susceptibility of a system $\chi$ to $\epsilon$ and is particularly suitable for a case where

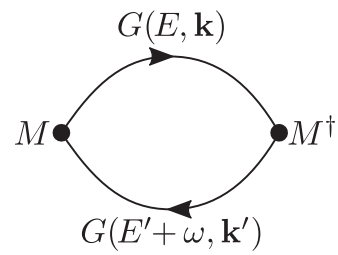


FIG. 3. The bubble diagram representing the density susceptibility, $\chi(\mathbf{q},\omega)$.

the main dynamics are due to mobile electrons [23]:

$$\epsilon(\mathbf{q},\omega) = 1 - \frac{4\pi e^2}{q^2}\chi(\mathbf{q},\omega), \tag{10}$$

where $\mathbf{q}$ and $\omega$ are the external wave vector and frequency, respectively. Since we seek $\epsilon(0,\omega_p) = 0$, this form reduces the problem to finding the long-wavelength limit of $\chi$.

Generally, $\chi$ can be expressed by a bubble diagram as in Fig. 3, through the Green's function of propagating particles in the system, $G(E,\mathbf{k})$ in Eq. (3), and the matrix element, $M = \langle \mathbf{k}, E|e^{i\mathbf{q}\cdot\mathbf{r}}|\mathbf{k}', E'\rangle$, which is on the vertex. Expressing $G$ through its spectral density using Lehmann representation [24], the bubble diagram represents the integral

$$\chi(\mathbf{q},\omega) = \frac{2}{\mathcal{V}}\int dE\, dE' \sum_{\mathbf{k}\mathbf{k}'} \frac{A_{\mathbf{k}}(E)A_{\mathbf{k}'}(E')|\langle \mathbf{k}, E|e^{i\mathbf{q}\cdot\mathbf{r}}|\mathbf{k}', E'\rangle|^2[f(E'-\mu) - f(E-\mu)]}{E' - E + \omega + i\eta}, \tag{11}$$

where $\mathcal{V}$ is the volume of the system, $f$ is the Fermi distribution, and $\eta$ is an infinitesimal positive energy. In writing Eq. (11), $\hbar$ is taken to be 1 and the factor of 2 accounts for spin degeneracy. In what follows, the denominator is always off resonance, so we set $\eta = 0$.

Using the sharp spectral density of Eq. (6), the $E$ and $E'$ integrals of Eq. (11) become trivial. In this case the bubble generates four separate terms, corresponding to four possible pairings of $a^+_{\mathbf{k}}$ and $a^-_{\mathbf{k}}$. Combining the cross terms together, we obtain three distinct contributions to the susceptibility:

$$\chi(\mathbf{q},\omega) = \chi_-(\mathbf{q},\omega) + \chi_+(\mathbf{q},\omega) + \chi_\times(\mathbf{q},\omega). \tag{12}$$

After standard manipulations to shift the origin of $\mathbf{k}$, these terms can be written as

$$\chi_\pm(\mathbf{q},\omega) = \frac{4}{\mathcal{V}}\sum_{\mathbf{k}\mathbf{k}'} \frac{a^\pm_{\mathbf{k}'}a^\pm_{\mathbf{k}}|\langle \mathbf{k}', \pm|e^{i\mathbf{q}\cdot\mathbf{r}}|\mathbf{k}, \pm\rangle|^2(E^\pm_{\mathbf{k}'} - E^\pm_{\mathbf{k}})f(E^\pm_{\mathbf{k}} - \mu)}{\omega^2 - (E^\pm_{\mathbf{k}'} - E^\pm_{\mathbf{k}})^2}, \tag{13}$$

$$\chi_\times(\mathbf{q},\omega) = \frac{4}{\mathcal{V}}\sum_{\mathbf{k}\mathbf{k}'} \frac{a^+_{\mathbf{k}'}a^-_{\mathbf{k}}|\langle \mathbf{k}', +|e^{i\mathbf{q}\cdot\mathbf{r}}|\mathbf{k}, -\rangle|^2(E^+_{\mathbf{k}'} - E^-_{\mathbf{k}})[f(E^-_{\mathbf{k}} - \mu) - f(E^+_{\mathbf{k}'} - \mu)]}{\omega^2 - (E^+_{\mathbf{k}'} - E^-_{\mathbf{k}})^2}, \tag{14}$$

where $|\mathbf{k}, \pm\rangle$ is the state with wave vector $\mathbf{k}$ in the $E_+$ or $E_-$ band. The $\chi_\pm$ terms correspond to intraband transitions, while $\chi_\times$ corresponds to interband transitions. We study the case where $\mu$ is in the $E^-_{\mathbf{k}}$ band, so $f(E^+_{\mathbf{k}} - \mu) = 0$ at low temperature, and $\chi_+$ can be neglected.

To find $\omega_p$, we need the $\mathbf{q} \to 0$ limit of Eq. (12). In Appendix A, we use a tight-binding model to argue that the matrix element $\langle \mathbf{k}, \pm|e^{i\mathbf{q}\cdot\mathbf{r}}|\mathbf{k}', \pm\rangle$ ensures momentum conservation, $\mathbf{k}' = \mathbf{k} + \mathbf{q}$. We also consider the leading-order terms as $\mathbf{q} \to 0$ and argue that for intraband transitions the leading term is simply 1, while in the case of interband transitions

$$\lim_{q\to 0}|\langle \mathbf{k}, -|e^{i\mathbf{q}\cdot\mathbf{r}}|\mathbf{k}', +\rangle|^2 \approx q^2 l^2 \delta_{\mathbf{k}',\mathbf{k}+\mathbf{q}} \tag{15}$$

for some length scale $l$. In principle, $l$ could be $\mathbf{k}$ dependent, but for simplicity we consider the case where $l$ is constant. In a tight-binding framework, $l$ is expected to be of the order of the lattice constant. We estimate the size of $l$ by showing that it is related to the matrix element in the interband absorption coefficient. We thus make an order-of-magnitude estimation of $l$ from transient absorption measurements on some HMAs [9]. That analysis is consistent with $l$ being of the order of a lattice constant for the host crystal.

Putting these results from Appendix A into Eqs. (13) and (14), for small $\mathbf{q}$,

$$\chi_-(\mathbf{q},\omega) = \frac{4}{\mathcal{V}}\sum_{\mathbf{k}} \frac{a^-_{\mathbf{k}+\mathbf{q}}a^-_{\mathbf{k}}(E^-_{\mathbf{k}+\mathbf{q}} - E^-_{\mathbf{k}})f(E^-_{\mathbf{k}} - \mu)}{\omega^2 - (E^-_{\mathbf{k}+\mathbf{q}} - E^-_{\mathbf{k}})^2} + O(q^3), \tag{16}$$

$$\chi_\times(\mathbf{q},\omega) = \frac{4q^2l^2}{\mathcal{V}}\sum_{\mathbf{k}} \frac{a^+_{\mathbf{k}}a^-_{\mathbf{k}}(E^+_{\mathbf{k}} - E^-_{\mathbf{k}})f(E^-_{\mathbf{k}} - \mu)}{\omega^2 - (E^+_{\mathbf{k}} - E^-_{\mathbf{k}})^2} + O(q^3). \tag{17}$$

We use these expressions to compute $\omega_p$ at low temperature by solving for $\epsilon(0,\omega_p) = 0$ in Eq. (10).

## III. PLASMA FREQUENCY OF DOPED HMA

If we take a parabolic form for the host CB, $E_{\mathbf{k}} = k^2/2m$, the small-$\mathbf{q}$ term in Eq. (16) can be calculated analytically. Details of the derivation are in Appendix B, and the result is

$$\frac{4\pi e^2\chi_-}{q^2} \approx \frac{\omega^2_{p0}}{\omega^2} = \frac{4e^2k_F^3}{3\pi m\omega^2}\left[\frac{1}{2}\left(1 - \frac{E_{k_F} - E_d}{\sqrt{(E_{k_F} - E_d)^2 + 4V^2x}}\right)\right]^3, \tag{18}$$

which defines $\omega_{p0}$, the plasma frequency when neglecting the interband transitions, which manifest through $\chi_\times$. Notice that without the cubed bracket, $\omega_{p0}$ would be the famous plasma frequency of an electron gas with Fermi momentum $k_F$. One can check that the bracket is in fact $a_k^-$, given in Eq. (7), and as we discuss further below, the presence of $(a_k^-)^3$ in $\omega_{p0}^2$ causes a nontrivial modification in the scaling of $\omega_p$ in HMAs.

Next, to represent the $\chi_\times$ contribution to the dielectric function, it is useful to define

$$\epsilon_\times(\omega) = 1 - \frac{4\pi e^2 \chi_\times}{q^2} = 1 + \frac{8e^2 l^2 V^2 x}{\pi} \int_0^{k_F} \frac{k^2 dk}{(E_k^+ - E_k^-)[(E_k^+ - E_k^-)^2 - \omega^2]}, \tag{19}$$

where the last equality uses the $\mathbf{q} \to 0$ limit of Eq. (17). While the integral in Eq. (19) cannot be evaluated in closed form, we see that it diverges if $\omega \geqslant E_\times$, where $E_\times$ is defined in Eq. (8). Due to this divergence, the $\omega$ dependence of $\epsilon_\times(\omega)$ is strongest when $\omega$ is close to $E_\times$, and numerical evaluation shows that for smaller $\omega$, $\epsilon_\times$ is only weakly dependent on $\omega$.

Setting $\epsilon = 0$ in Eq. (10) and using Eqs. (18) and (19), we find

$$\omega_p^2 = \frac{\omega_{p0}^2}{\epsilon_\times(\omega_p)}. \tag{20}$$

We now show how $\omega_p$ and $\omega_{p0}$ change with alloy fraction $x$ and doping, parametrized by $k_F$. Figure 4 shows $\omega_{p0}$ against $k_F$ for selected values of $V^2 x$. We normalize the $k_F$ axis using the natural inverse length scale, $k_d$, defined in Eq. (5). The $\omega_{p0}$ axis is normalized to $\omega_{pd}$, which is the plasma frequency of a free electron gas with effective mass $m$ when the Fermi momentum is equal to $k_d$; that is, $\omega_{pd} = \sqrt{4e^2 k_d^3/3\pi m}$.

When $E_d > 0$ (Fig. 4 top), $\omega_{p0}$ decreases with $x$ if $k_F < k_d$, while for higher filling $\omega_{p0}$ increases with $x$. For $k < k_d$, the lower band largely has the propagating character of the unperturbed CB, while for $k > k_d$, it is mostly made from the localized impurities, as seen in Fig. 1(b); this crossover causes the change in the behavior of $\omega_{p0}$ with $k_F$.

When $E_d < 0$ (Fig. 4 bottom), the $E_-$ band has largely localized impurity state character for all $k$, as shown in Fig. 2(b). In this case $\omega_{p0}$ increases with $x$ for all levels of filling. Note that in this case $\omega_{p0}$ is significantly smaller than $\omega_{pd}$ even for relatively large values of $V^2 x$; the lower share of propagating states in $E_-$ reduces the associated plasma frequency.

The plasma frequency including interband effects is given by the solution of Eq. (20), which can be found numerically. However, since the $\omega$ dependence of $\epsilon_\times(\omega)$ is only strong near $E_\times$, for $\omega_{p0}$ sufficiently smaller than $E_\times$ we can approximate the solution by $\omega_p \approx \omega_{p0}/\sqrt{\epsilon_\times(0)}$. But if $\omega_{p0}$ is near or larger than $E_\times$, then the diverging $\epsilon_\times(\omega)$ keeps the solution below $E_\times$. Therefore, $\omega_p$ is always smaller than both $\omega_{p0}$ and $E_\times$.

To show how $\omega_p$ is bounded by $\omega_{p0}$ and $E_\times$, Fig. 5 plots two example solutions of Eq. (20) against $V^2 x/E_d^2$. The top panel has $E_d > 0$ and the bottom has $E_d < 0$. The filling factor is taken to be the same in both cases, $k_F = 3k_d/4$. In order to make the bounding effects clearly visible, a rather large value for $\omega_{pd}$ has been chosen in the case of $E_d < 0$, corresponding to a case with $E_d$ just below the CB minimum. For $E_d > 0$ (top), $E_\times$ bounds $\omega_p$ for small $x$, while for $E_d < 0$ (bottom), it bounds $\omega_p$ for larger $x$.

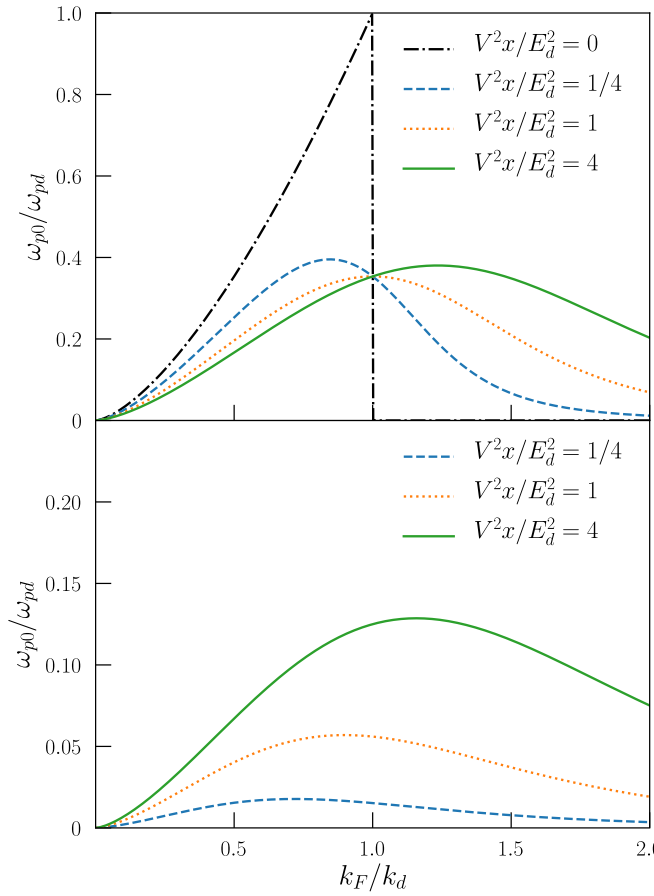


FIG. 4. Intraband plasma frequency $\omega_{p0}(k_F)$ of the $E_-$ band, according to Eq. (18) for selected values of $V^2 x/E_d^2$. The top panel has $E_d > 0$, and the bottom has $E_d < 0$. Increasing $x$ increases $\omega_{p0}$ when $E_d < 0$ and for heavily doped bands with $E_d > 0$, $k_F > k_d$. Contrastingly, increasing $x$ in lightly doped bands ($k_F < k_d$) with $E_d > 0$ decreases $\omega_{p0}$.

The differences between plasmons in HMAs and free electron gases can be seen in the low-density limit, when one might expect recovery of the free-electron result with a modified effective mass. In the low-density limit, the filled part of the $E_-$ band can be approximated by a parabolic band of effective mass $m_-$, given by

$$\frac{m}{m_-} = \frac{1}{2}\left(1 + \frac{E_d}{\sqrt{E_d^2 + 4V^2 x}}\right). \tag{21}$$

Also, for $k \ll k_d$ we find that $a_k^-$ in Eq. (7) becomes approximately independent of $k$ and approaches $m/m_-$, which we also call $a_-$. Moreover, the electron density in the HMA is $n = \int_0^{k_F} d\mathbf{k} a_\mathbf{k}^-/4\pi^3$, which means in this limit, $n \approx a_- k_F^3/3\pi^2$.

Then if $\omega_p$ had the standard scaling $\sqrt{n/m^*}$, it would scale as $a_-$, since $m_- \propto 1/a_-$ and $n \propto a_-$. However, $\omega_p$ in fact scales as $a_-^{3/2}$, which follows immediately from Eq. (18), where the quantity in brackets is $a_-$, as discussed previously.

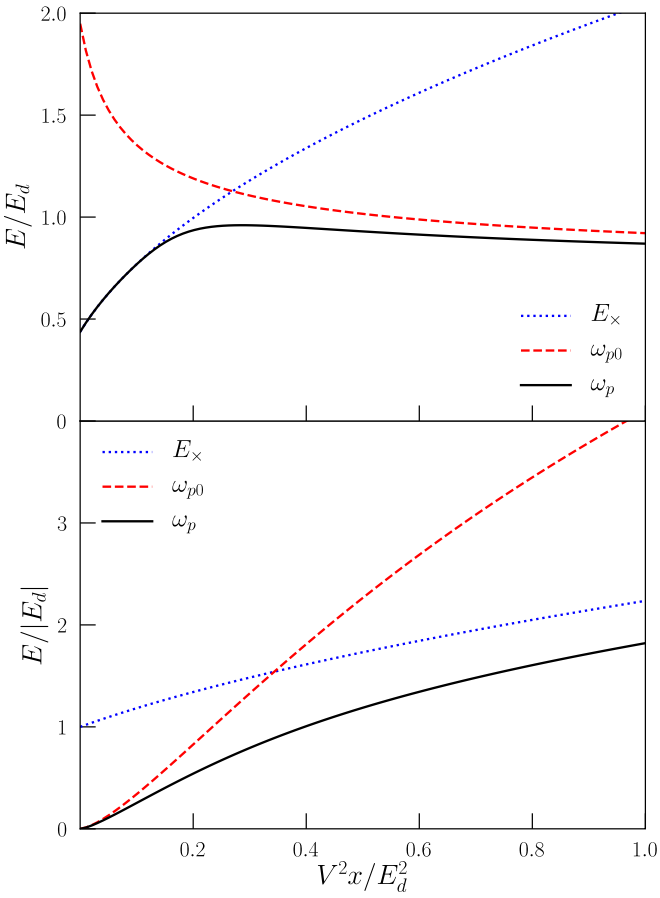


FIG. 5. Plasma frequency $\omega_p$ (solid lines) from numerical solution of Eq. (20) as a function of $V^2x/E_d^2$. The energy axis is normalized to $|E_d|$. $\omega_p$ is bounded below the intraband plasma frequency $\omega_{p0}$ (dashed lines), defined in Eq. (18), and the smallest interband gap $E_\times$ (dotted lines), defined in Eq. (8). The filling factor is $k_F = 3k_d/4$. Top: $E_d > 0$ with $\omega_{pd} = 3E_d$ and $l = 1/2k_d$. Bottom: $E_d < 0$ with $\omega_{pd} = 75|E_d|$, and $l = 1/10k_d$.

Note that in the low-doping regime, $\omega_p \approx \omega_{p0}$ because $\omega_{p0} \ll E_\times$ and $k_F$ is small enough that $\epsilon_\times \approx 1$.

This anomalous scaling can be observed in a set of HMAs with varying $x$ (which changes $a_-$ or equivalently $m_-$) in which doping ensures that $n$ is held constant. If $\omega_p$ with fixed $n$ obeyed the standard free-electron effective mass result, then as $x$ changes, $\omega_p$ would scale as $1/\sqrt{m_-} \sim \sqrt{a_-}$. Our theory instead predicts that in this fixed-$n$ case, $\omega_p$ in fact scales with $1/m_- \sim a_-$.

The unexpected extra factor of $\sqrt{a_-}$ in our result is due to the quadratic contribution of the weighting factor, $a_{\mathbf{k}}^-$, in the density susceptibility. This nontrivial scaling feature can be seen as a signature that reveals the density-density response mechanism that underlies the collective mode of plasma oscillations. Therefore, the special state distribution in HMAs carries a qualitative effect on their bulk plasma frequency all the way to the low-density limit. Since low levels of doping are most likely to be achievable in HMAs, we expect this peculiar scaling to be the most prominent prediction of our model to be checked by experiments.

TABLE I. Typical range of fixed parameters of BAC model for HMAs, where $m_e$ is the free electron mass.

| $E_d$ (eV) | $V$ (eV) | $m$ ($m_e$) |
|---|---|---|
| −0.6 to 0.4 | 1–3 | 0.02–0.15 |

## IV. EXPERIMENTAL SIGNATURES

In typical HMAs, in particular when the localized state couples to the CB of the host, the impurity level often falls within a few hundred meV below or above the CB edge. Considering that $V$ is generally of the order of a few eV, and with the typical light effective masses of the host CB in III-V and II-VI materials, $\hbar\omega_p$ can be as large as a few hundred meV. This scale suggests that a possible plasmonic material made by doping HMAs would operate in the range of mid-infrared or lower frequencies. Based on a limited review of the literature [1,9,25–39], Table I shows the typical range of the fixed parameters of the BAC model for III-V and II-VI HMAs with CB anticrossings.

To examine a realistic and flexible case, we consider the quaternary alloy $GaN_xP_yAs_{1-y-x}$. For this HMA we consider the nitrogen atoms to provide the localized states in a GaPAs host material. By varying the concentration of phosphorus, both positive and negative $E_d$ are realizable [28]. Transient absorption studies have been performed on two realizations of this alloy [9], which allows us to extract an estimate of the matrix element $l$ (see Appendix A). From those results, we estimate $l$ to be between 8 and 11 Å, and pick $l = 10$ Å for the following calculations. For the numerical values of $E_d$ and $V$, we rely on Ref. [28], and for the effective masses and the host's energy gaps we use Refs. [26,40]. For $V$ and $m$, we assume a linear interpolation with $y$. But for $E_d$, relying on Ref. [40], we also take into account bowing, $E_d(y) = (1-y)E_d|_{y=0} + yE_d|_{y=1} + y(1-y)C$, with $C = 0.19$ eV. These parameters are listed in Table II.

We consider moderately doped materials with fixed $n = 10^{18}$ cm$^{-3}$ and calculate $\omega_p$ by numerically solving Eq. (20), with results in Fig. 6 for all $y$ and $10^{-3} < x < 10^{-1}$. At this doping, $\hbar\omega_p$ is largest near the GaAs limit at small $y$ (i.e., positive $E_d$) and small $x$, approaching 120 meV. Here, $E_\times$ is always larger than 180 meV and hence does not have a significant bounding effect on $\omega_p$. The phosphorus fraction $y$ at which $E_d$ changes sign is marked on the plot. One can see that $\omega_p$ is generally smaller on the $E_d < 0$ side, where the $E_-$ band is predominantly made of the localized levels, and $a_-$ is generally small, similar to the results in Fig. 4.

Our simple two-band model for the dielectric function takes $\epsilon_\infty$ to be 1, which is not correct for most real materials. Based on that consideration, one would expect to find smaller

TABLE II. Parameters of BAC model for $GaN_xP_yAs_{1-y-x}$ [26,28,40], where $m_e$ is the free electron mass.

| Parameters | $y = 0$ | $y = 1$ |
|---|---|---|
| $E_d$ (eV) | 0.22 | −0.6 |
| $V$ (eV) | 2.8 | 3.05 |
| $m$ ($m_e$) | 0.067 | 0.13 |

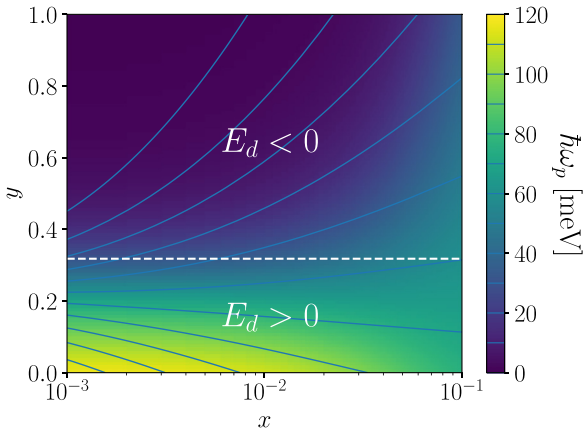


FIG. 6. Plasmon energy, $\hbar\omega_p$, for $GaN_xP_yAs_{1-y-x}$ at fixed electron density, $n = 10^{18}$ cm$^{-3}$. The BAC parameters listed in Table II, and explained in the text, are used for $GaN_xP_yAs_{1-y-x}$, and a fixed matrix element, $l = 10$Å, is assumed for the calculations. Plasma frequencies are highest below the dashed line, where $E_d$ is positive.

$\omega_p$ in an experiment than what we report here. The predictive nature of our model is in how $\omega_p$ changes upon changing of $x$ and doping, not the quantitative values.

Given that the plasmon resonance is expected to appear in the mid-infrared range, dielectric permittivity measurements such as ellipsometry [41] or Fourier-transform infrared spectroscopy [42,43] are viable candidates to extract $\omega_p$ in these materials. If the HMA supports plasmonic propagating modes, then indirect techniques such as the proposal in Ref. [44] can also give information on $\omega_p$.

The constraint that $E_\times$ imposes on $\omega_p$ could be important in certain cases. One would expect that effect to appear when $x$ is low, especially when $E_d$ is close to zero.

It is possible that $\omega_p$ for these materials may be close to their optical phonon resonance, especially in the low-doping regimes and when $E_d < 0$, when $\omega_p$ is small, as the typical frequency range of optical phonons is in terahertz. In such a case, one needs to be careful when extracting $\omega_p$ from permittivity measurements.

The great tunability of HMAs through both doping and alloy fraction allows for optimization of their potential plasmonic applications. In cases such as the quaternary $GaN_xP_yAs_{1-y-x}$, the relative location of the localized level can also be tuned, providing even more handles for tuning. Moreover, the gap between the $E_-$ and the $E_+$ bands could potentially allow for tuning the plasma frequency in a minimal loss regime [19], a fact that suggests the potential use of some well-tuned doped HMAs as low-loss plasmonic materials in the mid-infrared region.

The calculations presented in this work assume an infinitesimal broadening factor $\Gamma$ and ignore the disorder effects of the random alloy, which can allow violation of momentum conservation. Future work exploring the implications of these effects for plasmons may be important.

## ACKNOWLEDGMENTS

We acknowledge funding from the NSERC CREATE TOPSET program, Award No. 497981.

## APPENDIX A: LONG-WAVELENGTH LIMIT OF THE MATRIX ELEMENTS

Tight-binding (TB) models have been used to describe HMA band structure [28–30]. Here we use a TB model combined with experimental results to justify the long-wavelength approximation of the matrix element $|\langle \mathbf{k}, -|e^{i\mathbf{q}\cdot\mathbf{r}}|\mathbf{k}', +\rangle|^2$ in Eq. (15), including momentum conservation. In a TB model, wave functions in band $i$ are given by [45]

$$|\mathbf{k}, i\rangle = \frac{1}{\sqrt{N}} \sum_{\mathbf{R}} e^{i\mathbf{k}\cdot\mathbf{R}} \left|\phi_{\mathbf{k}}^{(i)}(\mathbf{r} - \mathbf{R})\right\rangle, \tag{A1}$$

where $\mathbf{k}$ is the crystal momentum, $\mathbf{r}$ is the position in the real space, and the sum is over all lattice points $\mathbf{R}$. $N$ is a normalization factor and, if we neglect overlaps between different sites, it is equal to the number of lattice points, while $\phi_{\mathbf{k}}^{(i)}$'s are an orthonormal set of orbital wave functions given by linear combinations of atomic (or molecular) orbitals of each unit cell. Using the form in Eq. (A1) we have

$$\begin{aligned}&\langle \mathbf{k}', i|e^{i\mathbf{q}\cdot\mathbf{r}}|\mathbf{k}, j\rangle \\ &\quad = \frac{1}{N} \sum_{\mathbf{R},\mathbf{R}'} e^{i(\mathbf{k}\cdot\mathbf{R} - \mathbf{k}'\cdot\mathbf{R}')} \left\langle \phi_{\mathbf{k}'}^{(i)}(\mathbf{r} - \mathbf{R}')\right| e^{i\mathbf{q}\cdot\mathbf{r}} \left|\phi_{\mathbf{k}}^{(j)}(\mathbf{r} - \mathbf{R})\right\rangle.\end{aligned} \tag{A2}$$

If we neglect the off-diagonal terms, $\mathbf{R} \neq \mathbf{R}'$, then multiply and divide Eq. (A2) by $e^{i\mathbf{q}\cdot\mathbf{R}}$, and shift $\mathbf{r} - \mathbf{R} \to \mathbf{r}$ in the matrix elements, we get

$$\begin{aligned}&\langle \mathbf{k}', i\left|e^{i\mathbf{q}\cdot\mathbf{r}}\right|\mathbf{k}, j\rangle \\ &\quad \approx \left\langle \phi_{\mathbf{k}'}^{(i)}(\mathbf{r})\right| e^{i\mathbf{q}\cdot\mathbf{r}} \left|\phi_{\mathbf{k}}^{(j)}(\mathbf{r})\right\rangle \frac{1}{N} \sum_{\mathbf{R}} e^{i(\mathbf{k}+\mathbf{q}-\mathbf{k}')\cdot\mathbf{R}} \\ &\quad = \left\langle \phi_{\mathbf{k}'}^{(i)}(\mathbf{r})\right| e^{i\mathbf{q}\cdot\mathbf{r}} \left|\phi_{\mathbf{k}}^{(j)}(\mathbf{r})\right\rangle \delta_{\mathbf{k}',\mathbf{k}+\mathbf{q}},\end{aligned} \tag{A3}$$

which immediately implies momentum conservation.

In the long-wavelength limit, we have $e^{i\mathbf{q}\cdot\mathbf{r}} \approx 1 + i\mathbf{q}\cdot\mathbf{r}$, and $\mathbf{k}' \approx \mathbf{k}$, due to momentum conservation. Therefore, the orthonormality of $\phi_{\mathbf{k}}^{(i)}$'s implies that the intraband matrix element is $|\langle \mathbf{k}', i|e^{i\mathbf{q}\cdot\mathbf{r}}|\mathbf{k}, i\rangle|^2 \approx \delta_{\mathbf{k}',\mathbf{k}+\mathbf{q}}$, while the interband matrix elements are

$$\langle \mathbf{k}', i\left|e^{i\mathbf{q}\cdot\mathbf{r}}\right|\mathbf{k}, j\rangle \approx i\mathbf{q}\cdot\left\langle \phi_{\mathbf{k}'}^{(i)}(\mathbf{r})\right|\mathbf{r}\left|\phi_{\mathbf{k}}^{(j)}(\mathbf{r})\right\rangle \delta_{\mathbf{k}',\mathbf{k}+\mathbf{q}}, \tag{A4}$$

as the first term vanishes due to orthogonality of $\phi_{\mathbf{k}}^{(i)}$'s. If a TB model with localized orbitals is a suitable model for describing the band structure of HMAs, then Eq. (A4) justifies the form that we choose in Eq. (15), suggesting that $l$ must be a length scale of the order of the lattice parameter.

The interband matrix element in Eq. (15) is related to the interband absorption, which permits an independent estimate of its magnitude. If $|s\rangle$ is an eigenstate of a system with energy $E_s$, the absorption coefficient is [46]

$$\alpha(E) = \frac{4\pi^2 e^2}{\overline{n}\hbar c E \mathcal{V}} \sum_{ss'} \left|\left\langle s\left|\frac{\hbar\hat{\mathbf{P}}}{m_e}\right|s'\right\rangle\right|^2 \delta(E_{s'} - E_s - E)(f_s - f_{s'}), \tag{A5}$$

where $\overline{n}$ is the refractive index and $\hat{\mathbf{P}}$ is the momentum operator.

It is also straightforward to see that if the only momentum dependence of a single-particle Hamiltonian is the kinetic part, $\mathbf{P}^2/2m_e$, as is the case for Hamiltonians describing band structures of crystals, then we have

$$(E_{s'} - E_s)\langle s|\mathbf{r}|s'\rangle = \frac{i\hbar}{m_e}\langle s|\mathbf{P}|s'\rangle, \tag{A6}$$

where $\mathbf{r}$ is the position operator. Equation (A6) shows how the position matrix element, as in Eq. (A4), is related to the momentum matrix element that is present in the expression of $\alpha$, Eq. (A5).

Assuming that $\hat{\mathbf{P}}$ also conserves momentum, the sum in Eq. (A5) reduces to a single sum over $\mathbf{k}$. Now consider that an $|s\rangle$, $|s'\rangle$ pair in Eq. (A5) are $|\mathbf{k}, \pm\rangle$, two eigenstates of the Hamiltonian in the $E_+$ and $E_-$ bands, respectively. Then the length scale $l$ is given by $|\langle \mathbf{k}, +|\mathbf{r}|\mathbf{k}, -\rangle|^2 = l^2$. Equation (A6) then allows $|\langle s|\hbar\mathbf{P}/m_e|s'\rangle|^2$ in Eq. (A5) to be written as $l^2E^2$, since the $\delta$ function enforces $E^+_{\mathbf{k}} - E^-_{\mathbf{k}} = E$.

With these considerations, and approximating that $l$ is independent of $\mathbf{k}$, for the $E_- \to E_+$ absorption coefficient we can write

$$\alpha(E) = \frac{4\pi^2 e^2 E l^2}{\bar{n}\hbar c} D_j(E), \tag{A7}$$

where $D_j(E)$ is the $\mathbf{k}$-conserving joint density of states with energy $E$.

In the transient absorption measurements of Ref. [9], photoexcitation populates the $E_-$ levels, and a probe beam is used to determine the absorption from these transiently populated states. We consider sample S205B, whose transient absorption spectrum 2 ps after photoexcitation is shown in their Fig. 3(a). We consider the absorption at $E = 0.8$ eV. Assuming that the absorption change is entirely due to the $E_- \to E_+$ transitions, and noting that the thickness of the absorptive layer is 0.5 $\mu$m, we estimate $\alpha(0.8\text{ eV}) \approx 700\text{ cm}^{-1}$.

Then, to use Eq. (A7) to estimate $l$, we need to estimate $D_j(E)$. First we calculate $D_j(E)$ between the full bands $E_-$ and $E_+$ while taking the weighting factors, $a_\pm$, into account. We then need to reduce $D_j(E)$ to account for the partial occupancy of $E_-$. Since the transient absorption experiment considers excitation from a photoexcited population in $E_-$ that is not in equilibrium, and since the $E_-$ bandwidth is not very wide, we consider the electrons to be uniformly distributed in $E_-$. We then reduce $D_j(E)$ by the ratio $n_-/n_{\max}$, where $n_-$ is the electron density in $E_-$, reported at 2 ps in Fig. 5 in Ref. [9] to be approximately $2 \times 10^{18}\text{ cm}^{-3}$. For $n_{\max}$, we consider two limiting approximations: first, $n_{\max} \approx 5.2 \times 10^{19}\text{ cm}^{-3}$ is the concentration of electrons in a completely filled $E_-$; second, $n_{\max} \approx 3.2 \times 10^{19}\text{ cm}^{-3}$ is the concentration of electrons in the $E_-$ band if it is filled up to the point where $E = 1.6$ eV (the upper limit of the observed $E_- \to E_+$ absorption band) is accessible. Using $\bar{n} = 3.25$ [47], these approximations produce a range for $l$ between 8 and 11 Å. Since in the particular case we are considering, interband transitions do not have a significant effect on plasma frequency, $\omega_p$ changes by at most about 3%, as $l$ varies between 8 and 11 Å. We use $l = 10$ Å in Fig. 6.

## APPENDIX B: ANALYTIC CALCULATION OF $\omega_{p0}$

In order to find $\omega_{p0}$ in Eq. (18), one needs to expand the $\chi_-$ integral in Eq. (16) up to second order, for a parabolic conduction band, $E_k = k^2/2m$. Performing the angular part of the integral, the first term in the expansion vanishes, and the next terms, which are proportional to $q^2$, have two parts,

$$\begin{aligned}\chi^{(2)}_-(q,\omega) = \frac{q^2}{8\pi^2 m\omega^2}\Bigg\{&\int_0^{k_F} k^2 \frac{[E_d - E_k + \sqrt{(E_k - E_d)^2 + 4V^2x}]^3}{[(E_k - E_d)^2 + 4V^2x]^{3/2}}dk \\ &- \frac{4V^2x}{m}\int_0^{k_F} k^4 \frac{[E_d - E_k + \sqrt{(E_k - E_d)^2 + 4V^2x}]^2}{[(E_k - E_d)^2 + 4V^2x]^{5/2}}dk\Bigg\} \\ = \frac{q^2}{8\pi^2 m\omega^2}&(I_1 - I_2),\end{aligned} \tag{B1}$$

where the last equation defines the integrals $I_1$ and $I_2$. Since $E_k = k^2/2m$, the change of variables $u = k^2$ allows integrating $I_1$ by parts to obtain

$$I_1 = \frac{k_F^3}{3}\left[1 - \frac{E_{k_F} - E_d}{\sqrt{(E_{k_F} - E_d)^2 + 4V^2x}}\right]^3 + I_2. \tag{B2}$$

Using this result in Eq. (B1) gives Eq. (18), which defines $\omega_{p0}$.


[1] W. Shan, W. Walukiewicz, J. W. Ager, E. E. Haller, J. F. Geisz, D. J. Friedman, J. M. Olson, and S. R. Kurtz, Phys. Rev. Lett. **82**, 1221 (1999).

[2] M. Weyers, M. Sato, and H. Ando, Jpn. J. Appl. Phys. **31**, L853 (1992).

[3] S. Nakamura and M. R. Krames, Proc. IEEE **101**, 2211 (2013).

[4] D. Friedman, J. Geisz, S. Kurtz, and J. Olson, J. Cryst. Growth **195**, 409 (1998).

[5] N. López, L. A. Reichertz, K. M. Yu, K. Campman, and W. Walukiewicz, Phys. Rev. Lett. **106**, 028701 (2011).

[6] N. Ahsan, N. Miyashita, M. M. Islam, K. M. Yu, W. Walukiewicz, and Y. Okada, Appl. Phys. Lett. **100**, 172111 (2012).

[7] M. Welna, M. Baranowski, W. M. Linhart, R. Kudrawiec, K. M. Yu, M. Mayer, and W. Walukiewicz, Sci. Rep. **7**, 44214 (2017).

[8] T. Tanaka, K. M. Yu, Y. Okano, S. Tsutsumi, S. Haraguchi, K. Saito, Q. Guo, M. Nishio, and W. Walukiewicz, IEEE J. Photovolt. **7**, 1024 (2017).

[9] J. N. Heyman, A. M. Schwartzberg, K. M. Yu, A. V. Luce, O. D. Dubon, Y. J. Kuang, C. W. Tu, and W. Walukiewicz, Phys. Rev. Appl. **7**, 014016 (2017).

[10] K. Zelazna, R. Kudrawiec, A. Luce, K.-M. Yu, Y. J. Kuang, C. W. Tu, and W. Walukiewicz, Sol. Energy Mater. Sol. Cells **188**, 99 (2018).

[11] J. N. Heyman, E. M. Weiss, J. R. Rollag, K. M. Yu, O. D. Dubon, Y. J. Kuang, C. W. Tu, and W. Walukiewicz, Semicond. Sci. Technol. **33**, 125009 (2018).

[12] A. Luque and A. Martí, Phys. Rev. Lett. **78**, 5014 (1997).

[13] W. Walukiewicz and J. M. O. Zide, J. Appl. Phys. **127**, 010401 (2020).

[14] R. H. Ritchie, Phys. Rev. **106**, 874 (1957).

[15] M. I. Stockman, Opt. Express **19**, 22029 (2011).

[16] G. V. Naik, V. M. Shalaev, and A. Boltasseva, Adv. Mater. **25**, 3264 (2013).

[17] T. Tanaka, K. Matsuo, K. Saito, Q. Guo, T. Tayagaki, K. M. Yu, and W. Walukiewicz, J. Appl. Phys. **125**, 243109 (2019).

[18] I. Kriegel, F. Scotognella, and L. Manna, Phys. Rep. **674**, 1 (2017).

[19] J. B. Khurgin and G. Sun, Appl. Phys. Lett. **96**, 181102 (2010).

[20] P. W. Anderson, Phys. Rev. **124**, 41 (1961).

[21] J. Wu, W. Walukiewicz, and E. E. Haller, Phys. Rev. B **65**, 233210 (2002).

[22] R. J. Elliott, J. A. Krumhansl, and P. L. Leath, Rev. Mod. Phys. **46**, 465 (1974).

[23] G. Giuliani and G. Vignale, in *Quantum Theory of the Electron Liquid* (Cambridge University Press, Cambridge, UK, 2005), pp. 188–274.

[24] H. Lehmann, Il Nuovo Cimento (1943-1954) **11**, 342 (1954).

[25] W. Walukiewicz, K. Alberi, J. Wu, W. Shan, K. M. Yu, and J. W. Ager, in *Dilute III-V Nitride Semiconductors and Material Systems: Physics and Technology*, edited by A. Erol (Springer, Berlin, 2008), pp. 65–89.

[26] S. Adachi, in *Properties of Semiconductor Alloys* (Wiley, New York, 2009), Chap. 6, pp. 133–228.

[27] K. M. Yu, W. Walukiewicz, J. Wu, W. Shan, J. W. Beeman, M. A. Scarpulla, O. D. Dubon, and P. Becla, Phys. Rev. Lett. **91**, 246403 (2003).

[28] R. Kudrawiec, A. V. Luce, M. Gladysiewicz, M. Ting, Y. J. Kuang, C. W. Tu, O. D. Dubon, K. M. Yu, and W. Walukiewicz, Phys. Rev. Appl. **1**, 034007 (2014).

[29] N. Shtinkov, P. Desjardins, and R. A. Masut, Phys. Rev. B **67**, 081202(R) (2003).

[30] E. P. O'Reilly, A. Lindsay, S. Tomić, and M. Kamal-Saadi, Semicond. Sci. Technol. **17**, 870 (2002).

[31] M. Seifikar, E. P. O'Reilly, and S. Fahy, J. Phys.: Condens. Matter **26**, 365502 (2014).

[32] P. Jefferson, T. Veal, L. Piper, B. Bennett, C. McConville, B. Murdin, L. Buckle, G. Smith, and T. Ashley, Appl. Phys. Lett. **89**, 111921 (2006).

[33] J. Wu, W. Shan, and W. Walukiewicz, Semicond. Sci. Technol. **17**, 860 (2002).

[34] A. Lindsay and E. O'Reilly, Solid State Commun. **112**, 443 (1999).

[35] A. Lindsay and E. O'Reilly, Solid State Commun. **118**, 313 (2001).

[36] C. Skierbiszewski, Semicond. Sci. Technol. **17**, 803 (2002).

[37] W. Walukiewicz, W. Shan, K. M. Yu, J. W. Ager, E. E. Haller, I. Miotkowski, M. J. Seong, H. Alawadhi, and A. K. Ramdas, Phys. Rev. Lett. **85**, 1552 (2000).

[38] I. Vurgaftman and J. R. Meyer, J. Appl. Phys. **94**, 3675 (2003).

[39] K. M. Yu, W. Walukiewicz, J. Wu, J. W. Beeman, J. W. Ager, E. E. Haller, W. Shan, H. P. Xin, C. W. Tu, and M. C. Ridgway, J. Appl. Phys. **90**, 2227 (2001).

[40] I. Vurgaftman, J. R. Meyer, and L. R. Ram-Mohan, J. Appl. Phys. **89**, 5815 (2001).

[41] D. Shah, H. Reddy, N. Kinsey, V. M. Shalaev, and A. Boltasseva, Adv. Opt. Mater. **5**, 1700065 (2017).

[42] P. Guo, R. D. Schaller, J. B. Ketterson, and R. P. Chang, Nat. Photonics **10**, 267 (2016).

[43] M. E. A. Panah, L. Han, K. Norrman, N. Pryds, A. Nadtochiy, A. Zhukov, A. V. Lavrinenko, and E. S. Semenova, Opt. Mater. Express **7**, 2260 (2017).

[44] T. Yang, J. Ge, X. Li, R. I. Stantchev, Y. Zhu, Y. Zhou, and W. Huang, Opt. Commun. **410**, 926 (2018).

[45] M. P. Marder, in *Condensed Matter Physics* (Wiley, New York, 2010), Chap. 8, pp. 207–232.

[46] M. P. Marder, in *Condensed Matter Physics* (Wiley, New York, 2010), Chap. 20, pp. 611–631.

[47] S. Adachi, in *Properties of Semiconductor Alloys* (Wiley, New York, 2009), Chap. 10, p. 323.